Journal of
Composites Science

MDPI

Article

Analytical Development of Impact Response of Stiffened Composite Panel with Optimum Structural Behaviour

José Juan Cruz Reyes and Hessam Ghasemnejad *

Aerospace and Aviation Theme, Cranfield University, Cranfield MK43 0AL, UK
* Correspondence: hessam.ghasemnejad@cranfield.ac.uk; Tel.: +44-(0)-123475-4395

Abstract

This paper presents an analytical framework for the preliminary design of stringer-stiffened composite panels subjected to low-velocity impact. The formulation combines First-Order Shear Deformation Theory with a two-degree-of-freedom spring–mass model, while the super-stringer is represented as a Euler–Bernoulli beam whose bending contribution is transferred to the skin mid-surface through the parallel axis theorem. This provides a computationally efficient tool for rapid parametric assessment of stiffened configurations at the early design stage. To support laminate selection, a Specific Impact Energy Index (SIEI) is introduced to rank configurations according to their elastic energy storage efficiency relative to the product of skin and stringer thicknesses. The tool is validated against both published experimental results and a finite element dynamic explicit model, demonstrating a good approximation of the impact response. It is then applied to identify the optimum laminate configuration for a super-stringer case study within the design space considered.

Keywords: impact; composites; spring-mass; stringer-stiffened panel

1. Introduction

The widespread adoption of Carbon Fibre Reinforced Polymer (CFRP) composites has fundamentally redefined structural design in the aerospace sector. Modern airframes, such as those of the Boeing 787 and Airbus A350, utilise these materials for over half of their primary structure due to their exceptional specific strength and stiffness compared to conventional aluminium alloys. Despite these technical advantages, the laminated and anisotropic nature of CFRPs introduces a critical vulnerability: a high susceptibility to out-of-plane loading, particularly low-velocity impact (LVI) events. Low-velocity impacts, typically caused by tool drops during maintenance or runway debris strikes, often result in internal damage that is not apparent upon visual inspection. This phenomenon, known as Barely Visible Impact Damage (BVID), is characterised by matrix cracking, fibre breakage, and interlaminar delamination. Such hidden degradation is particularly dangerous as it can lead to a catastrophic reduction in residual compressive strength, potentially causing premature buckling under service loads well below the design threshold. In the context of fuselage structures, this risk is exacerbated using stiffened panels. To maximise weight efficiency, thin skins are reinforced with longitudinal members, such as "Omega" or hat-shaped stringers. The interaction between the skin and the stringer creates a variable stiffness distribution that significantly complicates the impact response.

The analytical prediction of impact response in composite laminates began to consolidate in the 1970s and 80s. Early foundational work by Greszczuk et al. [1] formalised the application of Hertzian contact theory to anisotropic materials, establishing the role of

Check for updates

Academic Editor: Stelios K. Georgantzinos

Received: 18 March 2026
Revised: 4 April 2026
Accepted: 10 April 2026
Published: 16 April 2026

Copyright: © 2026 by the authors. Licensee MDPI, Basel, Switzerland. This article is an open access article distributed under the terms and conditions of the Creative Commons Attribution (CC BY) license.

contact stiffness in determining peak impact forces. A significant leap in modelling efficiency occurred when Shivakumar et al. [2] introduced the two-degree-of-freedom (TDOF) spring–mass system. By representing the impactor and the target as lumped masses connected by springs, they were able to predict force–time histories and impact durations with high accuracy for circular plates. Simultaneously, Tan et al. [3] demonstrated that static indentation laws could be effectively integrated into dynamic impact simulations, proving that for low velocities, the local deformation behaviour of a laminate is essentially quasi-static. As structural complexity increased, researchers turned their attention to reinforced panels. Gong et al. [4] developed analytical methods specifically for stringer-stiffened composite plates, highlighting how the stringer restricts global deformation and increases the peak contact force. The classification of impact regimes based on the mass ratio between the impactor and the plate was later refined by Olsson [5]. His research provided closed form solutions for predicting the delamination threshold energy, distinguishing between wave-controlled (small mass) and quasi-static (large mass) impacts. In the modern era, the focus has shifted toward balancing computational speed with physical accuracy. While Finite Element Analysis (FEA) provides high-fidelity results, its cost is often prohibitive for early-stage optimisation. Consequently, there has been a resurgence in refined analytical tools. For instance, Abdalla et al. [6] recently validated a MATLAB R2024b-based model using First Order Shear Deformation Theory (FSDT) and a TDOF approach, capturing the elastic response of unidirectional CFRP with errors as low as 1%.

The recent literature underscores the profound impact that LVI events have on the post-impact performance of stiffened structures. Experimental studies by Riming Tan et al. [7] found that an impact energy of only 23 J could cause serious fibre fracture and debonding in T-stiffened panels, leading to a reduction in buckling load and failure load by 9.62% and 34.1%, respectively. Similarly, Vescovini et al. [8] investigated tapered composite specimens, concluding that the distribution of transverse stiffness is the primary driver of energy absorption and damage resistance. Despite these advancements, a specific gap remains in the preliminary design phase: the identification of which elastic constants most influence the contact force in complex "super-stringer" configurations.

Despite these developments, a gap remains in the availability of analytical tools that can translate laminate-level constitutive properties into rapid impact-oriented design decisions for stiffened composite sub-assemblies. In particular, most existing reduced-order formulations are either focused on flat plates, rely on equivalent structural assumptions without an explicit laminate-to-stiffener reduction, or are not formulated for laminate ranking at the preliminary design stage.

The contribution of the present work is therefore not the introduction of FSDT or the spring–mass approach independently, but their integration into a laminate-driven analytical framework for stiffened panels. First, the stringer is reduced to explicit modal stiffness and modal mass contributions derived directly from its laminate properties and geometry, by shifting its bending rigidity to the skin mid-surface and projecting the result into the same modal basis as the skin. Second, this enables rapid parametric comparison of skin–stringer configurations using laminate stiffness quantities as direct inputs, without resorting to finite element simulations. Third, a Specific Impact Energy Index (SIEI) is proposed as a preliminary design metric to rank candidate configurations under fixed geometric and impact conditions.

2. Analytical Impact Modelling

The First Order Shear Deformation Theory (FSDT), also referred to as Mindlin–Reissner theory, extends the assumptions of Classical Laminate Theory by incorporating the effect of transverse shear deformation. While the classical formulation assumes that normals

to the mid-surface remain perpendicular after deformation, FSDT relaxes this condition, allowing these lines to rotate and remain straight but not necessarily orthogonal, as shown in Figure 1. This refinement becomes particularly relevant in the analysis of moderately thick laminates or when evaluating transverse shear effects in composite materials.

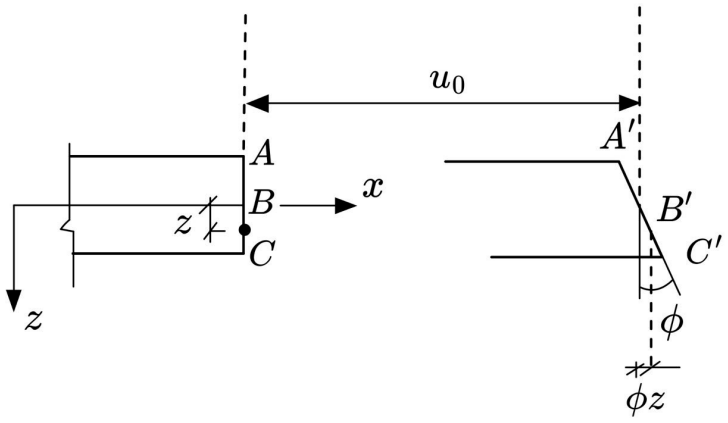

Figure 1. Deformed configuration FSDT assumptions.

In FSDT, the displacement field is augmented by including rotations of the normal about the in-plane axes. The in-plane displacements $u(x, y, z)$ and $v(x, y, z)$, and the transverse displacement $w(x, y)$, are defined as

$$u(x, y, z, t) = u_0(x, y, t) + z\psi_x(x, y, t), \tag{1}$$

$$v(x, y, z, t) = v_0(x, y, t) + z\psi_y(x, y, t), \tag{2}$$

$$w(x, y, t) = w_0(x, y, t), \tag{3}$$

where u_0, v_0, and w_0 are the displacements at the mid-surface and ψ_x, ψ_y are the rotations of the normal about the y and x axes, respectively. This formulation enables the model to capture transverse shear strains γ_{xz} and γ_{yz}, which are neglected in the Classical Laminate Theory.

FSDT is especially suitable for composite laminates, where the relatively low shear stiffness compared to in-plane stiffness can lead to significant deviations from classical behaviour. Its use is therefore recommended for structural elements of moderate thickness or when assessing impact response.

For a simply supported rectangular laminate of dimensions $a \times b$, the governing equations derived from FSDT can be further simplified by assuming negligible in-plane accelerations and rotary inertia effects. If perfect bonding between plies is assumed and the laminate exhibits specially orthotropic behaviour $\left(A_{16} = A_{26} = D_{16} = D_{26} = B_{ij} = 0\right)$ the equilibrium equations reduce to the coupled differential system:

$$D_{11}\frac{\partial^2\psi_x}{\partial x^2} + D_{66}\frac{\partial^2\psi_x}{\partial y^2} + (D_{12} + D_{66})\frac{\partial^2\psi_y}{\partial x\partial y} - k_{\text{sh}}A_{55}\left(\psi_x + \frac{\partial w}{\partial x}\right) = 0, \tag{4}$$

$$(D_{12} + D_{66})\frac{\partial^2\psi_x}{\partial x\partial y} + D_{66}\frac{\partial^2\psi_y}{\partial x^2} + D_{22}\frac{\partial^2\psi_y}{\partial y^2} - k_{\text{sh}}A_{44}\left(\psi_y + \frac{\partial w}{\partial y}\right) = 0, \tag{5}$$

$$k_{\text{sh}}A_{55}\left(\frac{\partial\psi_x}{\partial x} + \frac{\partial^2 w}{\partial x^2}\right) + k_{\text{sh}}A_{44}\left(\frac{\partial\psi_y}{\partial y} + \frac{\partial^2 w}{\partial y^2}\right) + q(x, y, t) = \rho h\frac{\partial^2 w}{\partial t^2}. \tag{6}$$

Here, $q(x, y, t)$ is the transverse load, h is the total laminate thickness, ρ is the material density and k_{sh} is the shear correction factor to compensate for the assumption of constant

transverse shear stress through the thickness, as this does not reflect the true parabolic distribution, typically taken as $\frac{\pi^2}{12}$. For specially orthotropic laminates, where coupling terms between bending and membrane actions vanish and transverse shear stiffnesses remain uncoupled, the shear behaviour is described using a reduced shear stiffness matrix $\left[A_{ij}\right]_s$. This matrix comprises only the terms A_{44} and A_{55}, associated with the shear moduli G_{13} and G_{23}, respectively. These values are obtained by integrating the shear stiffness contributions of each ply through the laminate thickness, as follows:

$$\left[A_{ij}\right]_s = \sum_{k=1}^{n} \left[\overline{Q_{ij}}\right]_s (z_k - z_{k-1}) \text{with} \left[\overline{Q_{ij}}\right]_s = \begin{bmatrix} G_{23} & 0 \\ 0 & G_{13} \end{bmatrix}. \tag{7}$$

The boundary conditions for a simply supported rectangular plate under a transverse load $q(x, y, t)$ are expressed as

$$w(x, y, t) = M_x(x, y, t) = 0 \quad \text{for } x = 0 \ \& \ x = a, \tag{8}$$

$$w(x, y, t) = M_y(x, y, t) = 0 \quad \text{for } y = 0 \ \& \ y = b. \tag{9}$$

To solve the coupled differential system given in (4)–(6), the displacement field and rotations are expressed using a double Fourier series expansion. This approach is particularly suitable for simply supported rectangular plates, as the boundary conditions are naturally satisfied by the chosen trigonometric basis functions. The displacement $w(x, y, t)$ and the rotations $\psi_x(x, y, t)$ and $\psi_y(x, y, t)$, are written as

$$\psi_x(x, y, t) = \sum_m \sum_n X_{mn}(t) \cos\left(\frac{m\pi x}{a}\right) \sin\left(\frac{n\pi y}{b}\right), \tag{10}$$

$$\psi_y(x, y, t) = \sum_m \sum_n Y_{mn}(t) \sin\left(\frac{m\pi x}{a}\right) \cos\left(\frac{n\pi y}{b}\right), \tag{11}$$

$$w(x, y, t) = \sum_m \sum_n W_{mn}(t) \sin\left(\frac{m\pi x}{a}\right) \sin\left(\frac{n\pi y}{b}\right), \tag{12}$$

and the external load $q(x, y, t)$ is similarly expanded as

$$q(x, y, t) = \sum_m \sum_n Q_{mn}(t) \sin\left(\frac{m\pi x}{a}\right) \sin\left(\frac{n\pi y}{b}\right). \tag{13}$$

In the case of a concentrated load applied at point (x_c, y_c), the loading coefficients $Q_{mn}(t)$ can be evaluated as

$$Q_{mn}(t) = \frac{4F(t)}{ab} \sin\left(\frac{m\pi x}{a}\right) \sin\left(\frac{n\pi y}{b}\right), \tag{14}$$

where $F(t)$ is the time dependent impact force. This formulation decouples the spatial and temporal dependencies of the governing equations, enabling their reduction to a system of linear ordinary differential equations in terms of the modal amplitudes $X_{mn}(t)$, $Y_{mn}(t)$, and $W_{mn}(t)$, driven by the loading coefficients $Q_{mn}(t)$ and determined by the laminate's stiffness properties:

By substituting the Fourier expansions (10)–(12) and (1) into the governing equations of motion (4)–(6) the system is transformed into a set of decoupled second order differential equations for each (m, n) mode. The resulting matrix form is given by

$$\left[L_{ij}\right] \begin{pmatrix} X_{mn} \\ Y_{mn} \\ W_{mn} \end{pmatrix} = \begin{pmatrix} 0 \\ 0 \\ \rho h \ddot{W}_{mn}(t) - Q_{mn}(t) \end{pmatrix}, \tag{15}$$

where $[L_{ij}]$ is the coefficient matrix of the system given by (4)–(6). This formulation allows treating each $(m,\ n)$ mode as an independent second order oscillator.

By observing the time dependent relation between $X_{mn}(t)$, $Y_{mn}(t)$ and $W_{mn}(t)$, it is possible to express the system response as a single second order differential equation for $W_{mn}(t)$, representative of a Single Degree of Freedom (SDOF) system:

$$\ddot{W}_{mn}(t) + \omega_{mn}^2 W_{mn}(t) = \frac{Q_{mn}(t)}{\rho h}. \tag{16}$$

This equation is formally equivalent to that of an SDOF oscillator with equivalent out of plane stiffness K, allowing for the identification of a modal frequency ω_{mn}. This analogy makes it possible to define an equivalent out-of-plane stiffness for the plate, that is, the relationship between a force applied at the centre of the plate and the resulting deflection at that same point, as expressed in Equation (16):

$$K = M^* \cdot \omega_{mn}^2. \tag{17}$$

In this formulation, the equivalent Rayleigh–Ritz mass of the plate M^*, is derived from the assumed deformed shape function. Since the present study deals with low-velocity impacts, the structural response is expected to be primarily governed by the first vibration mode, allowing higher-order modes to be neglected. Consequently, the equivalent Rayleigh–Ritz mass for a simply supported plate under transverse loading is defined as given in Equation (17):

$$M^* = \rho \cdot h \int_A \left(\sin\left(\frac{\pi x}{a}\right)\sin\left(\frac{\pi y}{b}\right)\right)^2 dA = \frac{M}{4}. \tag{18}$$

2.1. Spring–Mass Model for Impact

To analyse the impact behaviour of composite laminates, a simplified spring–mass model is adopted. This two-degree-of-freedom system models the interaction between the impactor and the target plate using two lumped masses connected by linear springs. The impactor is represented by mass M_2, while the equivalent mass of the plate is represented by M_1. The interaction is governed by two stiffness parameters: K_2, the contact stiffness at the interface between the impactor and the plate, and K_1, the equivalent bending stiffness of the simply supported laminated panel. A schematic of the model is shown in Figure 2.

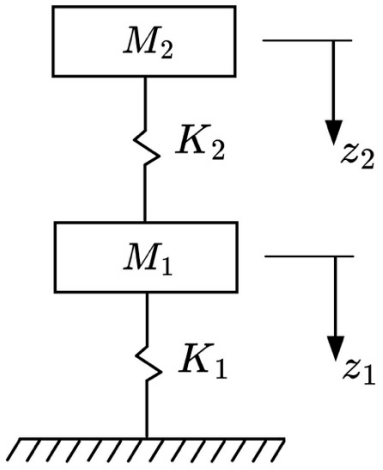

Figure 2. Spring–mass impact model scheme.

The core assumption of the model is that the contact deformation $\alpha(t)$, defined as the relative displacement between the impactor and the plate $(\alpha(t) = z2(t)z1(t))$, is small

and occurs over a short time scale. While Hertzian contact theory offers a non-linear formulation of the contact force as

$$F_c(t) = K_2(\alpha(t))^p, \tag{19}$$

where K_2 is the contact stiffness and p a contact constant, with $p = \frac{3}{2}$ for elastic contact. The current model adopts a linearised approach around the region of maximum deformation to ensure tractable analytical expressions. The resulting expression for contact force becomes

$$F_c(t) = K_2^* \alpha(t) = K_2^*[z_2(t) - z_1(t)], \tag{20}$$

where K_2^* is the effective linearised contact stiffness. This parameter is derived from the non-linear Hertzian form using material constants and geometric parameters of the impactor and target, as defined in

$$K_2^* = \sqrt{\pi}\,\Gamma\left(\frac{p+1}{2}\right)\frac{2\Gamma\left(\frac{p}{2}+1\right)+\sqrt{\pi}\,\Gamma\left(\frac{p+1}{2}\right)}{4\Gamma^2\left(\frac{p}{2}+1\right)+\pi\Gamma^2\left(\frac{p+1}{2}\right)}\,\alpha_m^{p-1}K_2, \tag{21}$$

where Γ denotes the Gamma function and α_m is the maximum contact deformation, calculated according to the boundary condition of the target plate. For free edge support, it is given by

$$\alpha_{m(f)} = \left(\frac{M_1 M_2}{M_1 + M_2}\right)^{0.4}\left(\frac{5V^2}{4K_2}\right)^{0.4}, \tag{22}$$

for clamped boundaries by

$$\alpha_{m(c)} = (M_2)^{0.4}\left(\frac{5V^2}{4K_2}\right)^{0.4}, \tag{23}$$

and for simply supported plates, as considered in this study, by taking the average between the two:

$$\alpha_{m(s)} = \frac{\alpha_{m(f)} + \alpha_{m(c)}}{2}. \tag{24}$$

The contact stiffness itself is computed using the improved Hertzian contact law:

$$K_2 = \frac{2}{3}\sqrt{R}\,\frac{E_2}{1-\nu_{23}^2}, \tag{25}$$

where ν_{23}^2 is the composite Poisson's ratio in the 23 planes, E_2 is the transversal Young's Modulus and R the spherical impactor ratio. The equivalent stiffness of the plate, K_1, is obtained from

$$K_1 = \omega_m^2 M_1, \tag{26}$$

with ω_m being the fundamental bending frequency of the laminated plate.

To determine the time history of contact force, the governing differential equations of the coupled spring–mass system are solved:

$$\begin{aligned} M_1\ddot{z_1} + (K_1 + K_2)z_1 - K_2 z_2 = 0, \\ M_2\ddot{z_2} - K_2 z_1 + K_2 z_2 = 0. \end{aligned} \tag{27}$$

Using initial conditions of zero displacement and plate velocity, and impactor velocity V, the system yields an analytical solution for the contact force in the form:

$$F_c(t) = K_2^*[A_1(C_1 - 1)\sin(\omega_1 t) + A_2(C_2 - 1)\sin(\omega_2 t)]. \tag{28}$$

The constants A_1, A_2, C_1, C_2 and the system frequencies ω_1, ω_2 are derived from the mass and stiffness ratios and represent the two vibrational modes of the coupled system: one in which the impactor and plate move in phase, and another in which they move out of phase. These are expressed analytically in Equations (29) and (30).

$$\omega_{1,2}^2 = \frac{1}{2}\left(\frac{K_1 + K_2^*}{M_1} + \frac{K_2^*}{M_2}\right) \mp \sqrt{\frac{1}{4}\left(\frac{K_1 + K_2^*}{M_1} - \frac{K_2}{M_2}\right)^2 + \frac{K_2^{*2}}{M_1 M_2}}, \tag{29}$$

$$C_1 = \frac{K_2^*}{K_2^* - \omega_1^2 M_2},\ C_2 = \frac{K_2^*}{K_2^* - \omega_2^2 M_2},\ A_1 = \frac{V}{\omega_1(C_1 - C_2)},\ A_2 = \frac{V}{\omega_2(C_2 - C_1)}. \tag{30}$$

The use of this simplified model allows efficient prediction of the force–time response during impact events. Despite the assumptions of linearisation and perfect contact, it provides a useful approximation for identifying trends in peak force and energy absorption, as explored in subsequent sections.

2.2. Stiffened Plate Model

The objective is to characterise, for a selected vibration mode ($m = 1$, $n = 1$), the equivalent modal stiffness K_{mn} and the equivalent modal mass M_{mn} of the system formed by a laminated skin and an attached stringer, what it can be named as super-stringer.

The skin is idealised as a rectangular plate of in-plane size $a \times b$ with all edges simply supported. A single stringer runs along the x direction (see Figure 3) and is located at the transverse coordinate $y = \frac{b}{2}$. Perfect bonding is assumed and the skin and the stringer share the same transverse deflection along the stringer line. This assumption implies that no interfacial slip or debonding occurs during the impact event. Accordingly, the present formulation is intended to represent the intact structural response, or equivalently the early stage of impact before significant skin–stringer interface degradation develops.

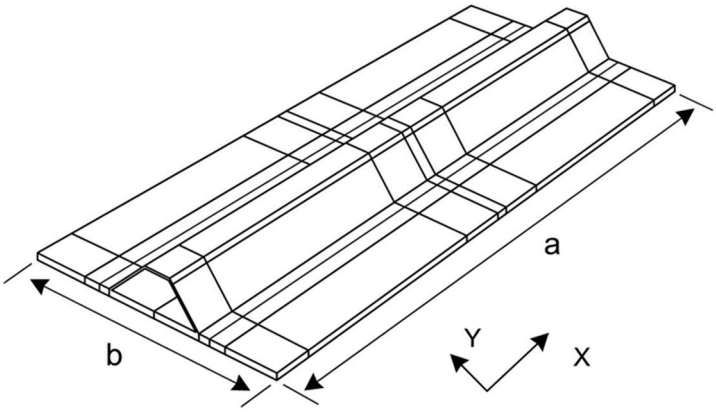

Figure 3. Geometry of the super-stringer.

The plate kinematics are described by FSDT. A single admissible mode is adopted to separate space and time

$$w(x, y, t) = W_{mn}(t) \sin\left(\frac{m\pi x}{a}\right) \sin\left(\frac{n\pi y}{b}\right), \tag{31}$$

which is appropriate for low-velocity impacts where the fundamental response dominates. The analysis is carried out in the linear regime with small strains and small rotations, and laminae are modelled as linearly elastic orthotropic materials.

Under these assumptions, the internal energies are additive. In a single-mode setting, this implies that the modal contributions of the skin and the stringer accumulate into the global stiffness and mass of the assembled system.

So far, we know how to compute the stiffness of a laminate with simply supported boundary conditions. However, in this case we must determine how to model the stiffness of the super-stringer configuration. By kinematic compatibility and assuming perfect bonding, the in-plane displacement of the stringer and the skin must be identical within the bonded region. Consequently, the deflection profile along the x-axis for the panel without a stringer follows the qualitative trend indicated by the black dashed line in Figure 4, whereas the blue dashed line corresponds to the deformed shape of the panel with a stringer.

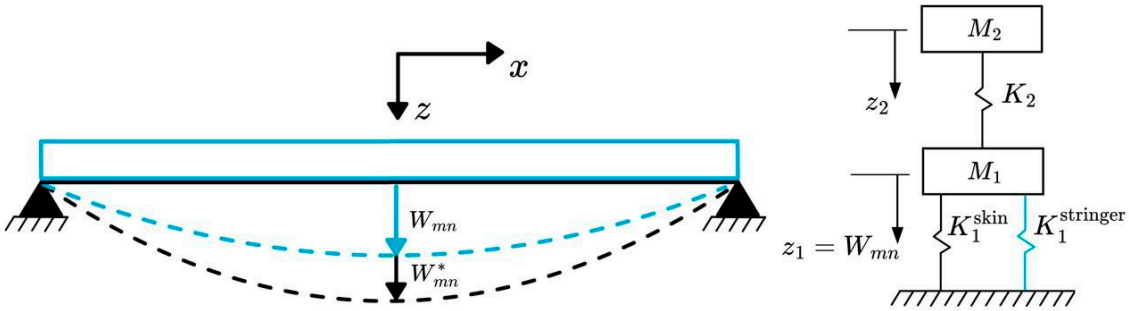

Figure 4. Super-stringer panel equivalent spring model.

Since one of the primary roles of a stringer is to increase bending stiffness about the y-axis, the presence of the stringer reduces the modal amplitudes relative to the unstringered case and therefore leads to a smaller maximum deflection than the configuration without a stringer ($W_{mn} < W^*_{mn}$). Because the stringer and the skin must exhibit identical displacement within the bonded region (perfect bonding), and since the stringer increases the overall stiffness, the natural choice for the equivalent spring–mass representation is the configuration shown on the right of Figure 4, namely with the springs arranged in parallel.

The next step is therefore to determine the stiffness of the stringer, denoted as K^{stringer}. The stringer is idealised as an Euler–Bernoulli beam aligned with the x-axis and located at $y = \frac{b}{2}$. This choice is appropriate for a slender stiffener spanning a length $L = a$ with $L/d^{\text{stringer}} \geq 10 \sim 15$, where d^{stringer} denotes the effective depth (overall height) of the stringer cross-section.

Although the omega-shaped geometry forms a closed section and may therefore possess non-negligible torsional rigidity, torsional effects are not included in the current low-fidelity model. This simplification is considered acceptable for the centrally applied transverse impact studied here, where the dominant structural response is bending-driven. However, for off-centre impacts or loading cases inducing significant twist, the omission of torsional rigidity may reduce the fidelity of the prediction.

The mechanical characterisation follows from the stringer laminate and its geometry, with the axis convention that the 0° ply direction is perpendicular to the stringer. Hence, the material direction 2 is parallel to the stringer, and the bending rigidity relevant to curvature along the stringer is the component D_{22}. The laminate bending term is first shifted to the skin mid-surface through the geometric offset:

$$z_0 = \frac{h_{\text{skin}}}{2} + \frac{h^*_{\text{stringer}}}{2}, \tag{32}$$

where h_{skin} is the skin thickness and h^*_{stringer} is an effective height of the stringer over its footprint. For webs inclined by an angle θ, measured with respect to the vertical z-axis, conservation of the real stringer area over its projection on the plate (top view) leads to

$$h^*_{\text{stringer}} = h_{\text{stringer}} \frac{l_{\text{cap}} + 2\,l_{\text{web}}/\cos(\theta)}{l_{\text{cap}} + 2\,l_{\text{web}}}. \tag{33}$$

The factor $\frac{1}{\cos(\theta)}$ appears because the web thickness must be projected onto the y direction to conserve area when the web plane is rotated in the $y-z$ plane. Before introducing the shifted bending term, it is useful to recall the general transformation of the laminate stiffness matrices when the reference plane is changed. As expressions for the laminate stiffness matrices, referred to a generic origin $z=0$, are defined as

$$A = \int Q\,dz, \quad B = \int z\,Q\,dz, \quad D = \int z^2\,Q\,dz, \tag{34}$$

if the reference plane is shifted to a new plane located a distance Δ from the original one, the new coordinate becomes $\zeta = z\Delta$. The transformed stiffness matrices, expressed in the new coordinate system, are then

$$\begin{aligned} A' &= \int Q\,d\zeta = \int Q\,dz = A, \\ B' &= \int \zeta\,Q\,d\zeta = \int (z-\Delta) Q\,dz = B - \Delta A, \\ D' &= \int \zeta^2 Q\,d\zeta = \int (z-\Delta)^2 Q\,dz = \int \left(z^2 - 2\Delta z + \Delta^2\right) Q\,dz = D - 2\Delta B + \Delta^2 A. \end{aligned} \tag{35}$$

This shows that only the B and D matrices depend on the position of the reference plane, since they contain terms proportional to z and z^2, respectively. Applying this transformation to the laminate of the stringer, with $\Delta = z_0$ defined in Equation (32) the bending stiffness referred to the skin mid-surface becomes

$$D'_{22} = D_{22} - 2\,z_0\,B_{22} + z_0^2\,A_{22}. \tag{36}$$

The quantity D'_{22} represents the stringer's bending rigidity per unit width measured about the skin mid-surface and accounts for the geometric offset between centrelines.

This plate-type rigidity per unit width is mapped to a beam bending stiffness via an effective footprint width in the y direction.

$$EI_y = D'_{22}\,l_{eff}, \tag{37}$$

with

$$l_{\text{eff}} \approx l_{\text{cap}} + 2\,l_{\text{web}}, \tag{38}$$

which is the top view footprint of cap and webs on the plate.

The stringer mass enters as a line mass $\mu = \rho_{\text{st}} A_{\text{sec}}$ along x, where ρ_{st} and A_{sec} denote the effective density and the real cross-sectional area. With EI_{y} and μ defined in terms of laminate data and geometry, the subsequent subsections derive the closed form modal contribution of the stringer and show how it enters the assembled stiffness K^{stringer} to be combined with the skin contribution.

Within the Euler–Bernoulli idealisation, the stringer is assumed perfectly bonded to the skin and therefore follows the plate's transverse deflection along its line at $y = y_s$. Its motion is thus governed by the same admissible mode previously introduced in Equation (31) and the stringer's contribution can be obtained by projecting its bending energy and kinetic energy onto that modal field.

The bending strain energy of the stringer reads

$$U_{\text{stringer}} = \frac{1}{2}\int_0^a EI_y \left(\frac{\partial^2 w}{\partial x^2}\right)^2 dx, \tag{39}$$

using Equation (31) one has

$$\frac{\partial^2 w}{\partial x^2} = -\left(\frac{m\pi}{a}\right)^2 W(t) \sin\left(\frac{m\pi x}{a}\right) \sin\left(\frac{n\pi y_s}{b}\right), \tag{40}$$

as $y_s = \frac{b}{2}$ and $n = 1$, then $\sin\left(\frac{n\pi y_s}{b}\right) = 1$. In addition, $\int_0^a \sin^2\left(\frac{m\pi x}{a}\right) dx = \frac{a}{2}$. Then, substitution gives

$$U_{\text{stringer}} = \frac{1}{2}\left[EI_y \left(\frac{m\pi}{a}\right)^4 \frac{a}{2} \right] W^2, \tag{41}$$

so that, by identification with $U = \frac{1}{2}KW^2$ and with $m = 1$, the stringer modal stiffness is

$$K_1^{\text{stringer}} = EI_y \left(\frac{\pi}{a}\right)^4 \frac{a}{2} = \frac{D'_{22}\, l_{\text{eff}} \pi^4}{2a^3}. \tag{42}$$

On the other hand, the kinetic energy of the stringer is

$$T_{\text{stringer}} = \frac{1}{2}\int_0^a \mu \left(\frac{\partial w}{\partial t}\right)^2 dx = \frac{1}{2}\mu \dot{W}^2 \int_0^a \sin^2\left(\frac{m\pi x}{a}\right) dx, \tag{43}$$

which yields in

$$T_{\text{stringer}} = \frac{1}{2}\left[\mu \frac{a}{2} \right] \dot{W}^2. \tag{44}$$

Matching $T = \frac{1}{2}M\dot{W}^2$, gives the stringer modal mass:

$$M_1^{\text{stringer}} = \mu \frac{a}{2}. \tag{45}$$

Denote by K_1^{skin} and M_1^{skin} the modal stiffness and mass of the skin and by K_1^{stringer} and M_1^{stringer} the closed form contributions of the stringer derived here, the assembled modal quantities are

$$K_1 = K_1^{\text{skin}} + K_1^{\text{stringer}} \text{and } M_1 = M_1^{\text{skin}} + M_1^{\text{stringer}} \tag{46}$$

In particular, using the Euler–Bernoulli stringer expressions

$$K_1 = K_1^{\text{skin}} + \frac{D'_{22}\, l_{eff} \pi^4}{2a^3}, \tag{47}$$

$$M_1 = M_1^{\text{skin}} + \mu \frac{a}{2}. \tag{48}$$

These assembled parameters (K_1, M_1), together with the impactor mass M_2 and the contact stiffness M_2, define the two-degree-of-freedom impact system used to compute the contact force history.

An important feature of this formulation is that the stiffener contribution is obtained in closed form from laminate constitutive properties and geometric descriptors, rather than through numerical calibration or an equivalent flat-panel approximation alone. This provides a direct laminate to structure link within the impact model, allowing the influence of stringer layup and thickness to be assessed within the same analytical framework as the skin. As a result, the method is particularly suitable for preliminary parametric studies, where a large number of skin-stringer combinations must be screened efficiently before higher-fidelity numerical analysis.

3. Theoretical Model Validation

To establish confidence in the analytical framework presented in Section 2.1, the model is validated against published results reported by Vaziri et al. [9] for a specific laminate and impact scenario, where the reference data are based on the experimental campaign of Delfosse et al. [10]. The objective is to verify that the predicted force–time history and derived quantities are consistent with reference data when identical geometric, material

and loading conditions are used Tables 1 and 2 summarises the laminate and impactor data used to replicate the reference case.

Table 1. CFRP lamina properties with $[45/90/-45/0]_{3s}$ stacking sequence.

E_1 [GPa]	E_2 [GPa]	G_{12} [GPa]	ν_{12} [-]	ρ [kg/m^3]	Laminate Dimensions [mm]
129	7.5	3.5	0.33	1540	$12.7 \times 7.62 \times 4.65$

Table 2. Spherical impactor properties.

R [mm]	E [GPa]	ν [-]	M [kg]
12.7	207	0.3	6.14

Figure 5 shows that the analytical model captures the correct order of magnitude and overall duration of the impact event, although differences remain in the waveform shape. In particular, the analytical force history exhibits an oscillatory pattern, whereas the reference experimental curve is smoother. This behaviour is a direct consequence of the two-degree-of-freedom spring–mass formulation, in which the contact force results from the superposition of two natural modes. When both modal contributions have comparable amplitudes and distinct frequencies, a beat-like oscillatory response appears. It should also be noted that this discrepancy is partly explained by the treatment of the reference data in the literature. As reported by Vaziri et al. [9], the particular numerical time integration adopted in their work damped out multiple high-frequency oscillations in the predicted force–time histories, and the experimental data from Delfosse et al. had also been filtered to remove part of this oscillatory content as high-frequency noise. Therefore, the smoother waveform in the reference results does not necessarily imply the absence of oscillatory behaviour in the actual structural response. To enable a more realistic comparison, the analytical force history has also been filtered before plotting, reducing part of the high-frequency oscillatory content while preserving the main response trend. For this reason, validation should not rely only on visual agreement of the force history, but also on quantitative indicators such as peak force ($F_{\max}$) and contact duration (t_c).

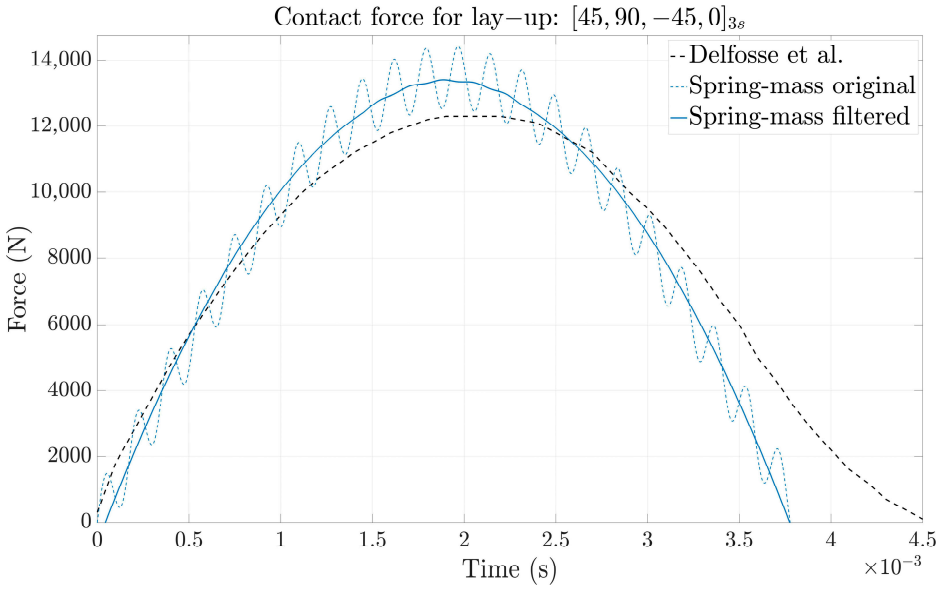

Figure 5. Force history comparison of the laminate model with V = 2.68 m/s [10].

To quantify the predictive capability of the model, Table 3 compares the analytical and experimental values of F_{max} and t_c. Although the waveform shape differs, the model reproduces the key engineering indicators with acceptable accuracy for preliminary design purposes, with a difference of 8.3% in peak force and 16% in contact duration.

Table 3. Quantitative comparison between analytical filtered prediction of the laminate model and experimental results.

	F_{max} [N]	t_c [ms]
Experimental	12,300	4.5
Analytical	13,413.86	3.78

Since no experimental data are currently available for the specific super-stringer configuration considered in this work, the stiffened-panel results are compared against a high-fidelity Abaqus/Explicit model (see Figure 6) as a numerical reference. This comparison should therefore be interpreted as a numerical corroboration of the analytical formulation, rather than as a full experimental validation. The finite element reference model was implemented in Abaqus/Explicit using a three-dimensional discretisation of both the impactor and the stiffened laminate. The spherical striker was meshed with 8-node linear brick elements (C3D8), while the super-stringer was modelled using 8-node continuum shell elements (SC8R), which are well suited to capture the through-thickness behaviour of laminated composites at moderate computational cost. Contact between the striker and the composite panel was defined using a hard normal contact formulation with frictionless tangential behaviour. No viscous regularisation was introduced, in order to avoid artificial damping effects on the force–time history. Likewise, no mass scaling was applied, so that the dynamic response remained governed by the physical inertia of the system rather than by numerical acceleration techniques.

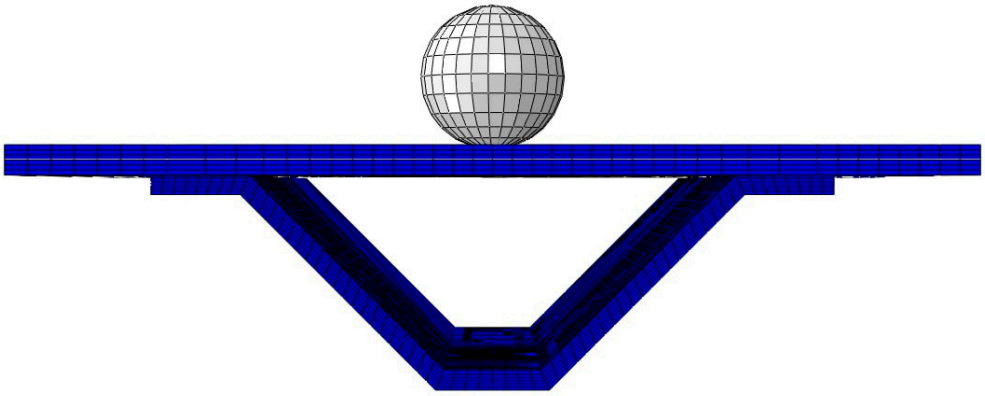

Figure 6. Model setup in Abaqus/explicit.

The results were obtained using the same material properties and stacking sequence as those listed in Tables 1 and 2 for both the laminate and the impactor, except that the laminate dimensions are now 15 × 10 × 4.65 mm. As for the super-stringer, the same material properties and stacking sequence as those of the laminate were adopted, but with a thickness of 3 mm. The results obtained are presented below:

In the case of Figure 7, a certain oscillatory behaviour can also be identified in the FEM force history, although its amplitude is considerably smaller than in the analytical prediction and it is mainly confined to the early stage of the response. This suggests that the oscillatory content is not exclusively an artefact of the present analytical model, but rather a feature that may arise in dynamic impact simulations depending on modal participation,

contact treatment and numerical resolution. Nevertheless, the smoother character of the FEM curve indicates that the analytical spring–mass formulation tends to amplify this modal interaction more strongly than the finite element model. For this reason, the FEM comparison is used here primarily to verify whether the analytical framework reproduces the correct force level, response scale and main trends, rather than to demonstrate exact agreement in waveform shape.

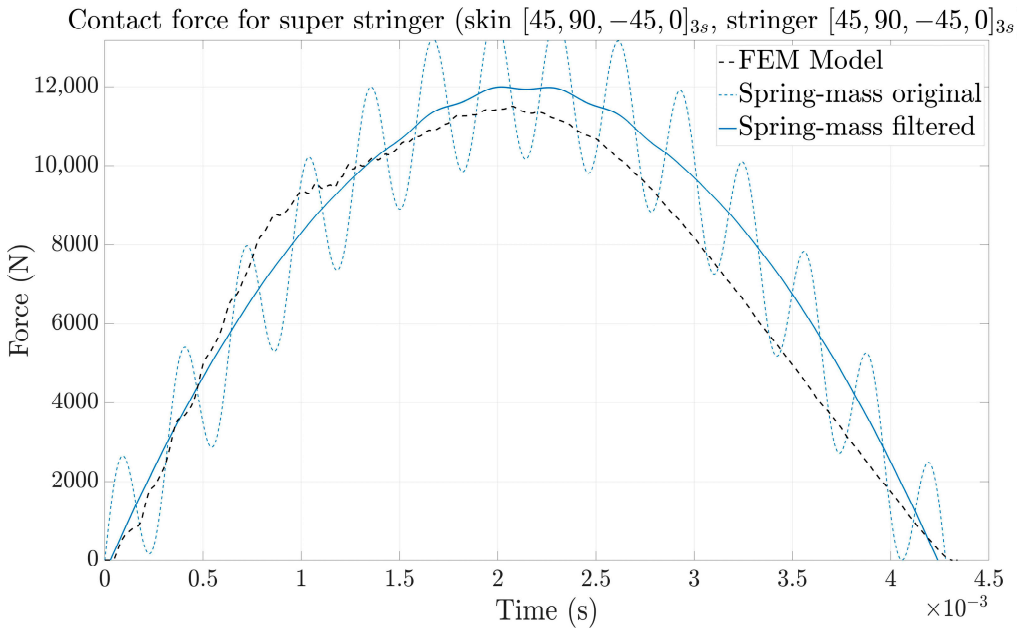

Figure 7. Force history comparison of the super-stringer model with V = 2.68 m/s.

Table 4 evaluates the model performance by contrasting the analytical predictions of $F_{\max}$ and t_c with the corresponding FEM results. Despite the discrepancies in the overall waveform profile, the model provides a reasonably accurate estimate of the parameters of greatest engineering interest at the preliminary design stage, with errors of 4.04% for the maximum force and 1.61% for the contact time.

Table 4. Quantitative comparison between analytical filtered prediction of the super-stringer model and FEM results.

	$F_{\max}$ [N]	t_c [ms]
FEM	11,513.55	4.34
Analytical	11,997.94	4.27

It is also important to note that the FEM results, like the present analytical predictions, do not represent reality exactly, but constitute a numerical approximation subject to their own modelling assumptions and limitations, including discretisation effects, contact definitions, material idealisations and the lack of experimentally calibrated damage evolution for the stiffened configuration.

4. Configuration Designs

To identify the most suitable laminate for the super-stringer, a clear selection criterion is required. Since the design objective is not simply to maximise stiffness or peak load, but rather to promote the highest possible impact damage absorption at the lowest possible structural mass, the laminate must be assessed based on structural efficiency rather than absolute response alone. In practice, a heavier configuration may absorb more total

energy simply because it contains more material, yet this would be inconsistent with the lightweight philosophy that governs aerospace structures. Therefore, by analogy with the specific energy absorption criteria commonly adopted in crashworthiness and energy-absorbing structure design, the most suitable laminate is the one that provides the greatest damage-absorption capability per unit mass. On this basis, we define the following metric, termed the Specific Impact Energy Index (SIEI):

$$\mathrm{SIEI} = \frac{E_c}{h_{\mathrm{skin}}\, h_{\mathrm{stringer}}}, \tag{49}$$

the energy E_c represents the elastic energy stored in the contact system during loading, and is computed as the work done by the contact force up to maximum deformation:

$$E_c = \int_0^{\alpha_{\max}} F_c(\alpha)\, d, \tag{50}$$

for a linearised contact model with stiffness K_2^*, the force-deformation relation is the one in Equation (20) and the integral simplifies to

$$E_c = \frac{1}{2} K_2^* \alpha_{\max}^2. \tag{51}$$

It should be noted that E_c corresponds to recoverable elastic energy within the present low-fidelity framework, since the model does not include explicit damage evolution or irreversible dissipation. Therefore, the proposed SIEI is not intended as a universal measure of damage resistance or damage tolerance. Instead, it is introduced here as a comparative design index for fixed geometry, boundary conditions and impact velocity, allowing candidate configurations to be ranked according to their elastic energy storage efficiency penalised by total thickness.

That said, the following can be used:

$$\mathrm{SIEI} = \frac{K_2^* \alpha_{\max}^2}{2 h_{\mathrm{skin}}\, h_{\mathrm{stringer}}}. \tag{52}$$

In this study all remaining geometric dimensions of the super-stringer are fixed and all comparative assessments are conducted for a nominal impact velocity of 3 m/s and the properties from Table 2. The selection is performed in two stages: first, the stacking sequence is chosen based on the performance metric; second, once the layup is fixed, the laminate thicknesses are determined to maximise SIEI subject to the stated constraints.

It should be noted that the SIEI is not intended as a universal impact-performance metric. In the present study, it is introduced as a configuration-specific screening index for preliminary design, valid under the assumptions of fixed geometry, fixed boundary conditions and a prescribed nominal impact velocity. Within this scope, it provides a practical means of comparing candidate laminates according to stored elastic impact energy penalised by thickness, so that higher SIEI values indicate configurations that store more recoverable impact energy per unit thickness and are therefore more efficient from a preliminary design perspective. For other applications or design objectives, the normalisation may require reformulation, particularly when damage propagation or post-impact residual strength are dominant concerns, in which case the metric should be extended to include dissipated energy or stiffness degradation.

These are the four stacking sequence options for this study as shown in Table 5.

Table 5. Stacking sequences.

Layup 1	$[60/-60/0/90]_{3s}$	Layup 2	$[45/90/-45/0]_{3s}$
Layup 3	$[0/90/90/0]_{3s}$	Layup 4	$[45/-45/0/90]_{3s}$

It is important to recall that a super-stringer must not only tolerate impact but also provide longitudinal stability against panel buckling. From the stringer's standpoint this favours fibre alignment along its axis, hence a higher proportion of plies at 0° with respect to the stringer axis. In the present formulation the 0° direction is defined perpendicular to the stringer; therefore, axial alignment corresponds to 90° plies. Consequently, among the four candidate stacking sequences considered, the layup 3 is the most suitable one for the stringer. Furthermore, by plotting the SIEI against the skin ply thickness for each of the four skin stacking sequence options, it is possible to identify the optimum stacking sequence for the skin.

The results in Figure 8 show that the skin stacking sequence has a clear influence on the structural efficiency measured through the SIEI. Among the four candidates, Layup 4, $[45/-45/0/90]_{3s}$, consistently provides the highest SIEI over the whole range of skin ply thicknesses, and therefore represents the most suitable skin layup for the super-stringer configuration. The trend observed indicates that increasing the skin thickness initially improves the energy absorption capability faster than the associated thickness penalty, but beyond a certain point the added material no longer produces a proportional gain in absorbed energy, causing the SIEI to decrease. From the present plot, the optimum skin ply thickness appears to lie around $t_{\text{skin}} \approx 0.35$ mm. However, this optimum is only valid for the specific stringer configuration considered here, namely a total stringer thickness of 3 mm corresponding to a ply thickness of 0.125mm. Therefore, once the optimum skin stacking sequence has been identified as Layup 4, the remaining task is to determine the combined optimum values of skin and stringer ply thicknesses. For this reason, the next step is to plot the SIEI as a function of both t_{skin} and t_{stringer} for the selected skin layup.

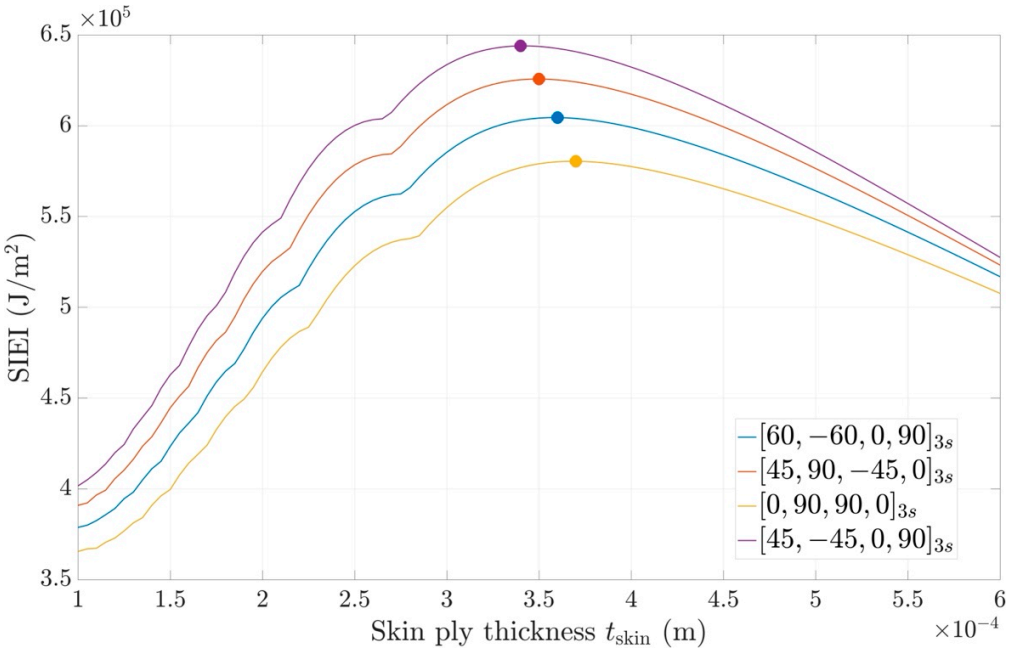

Figure 8. SIEI with skin ply thickness with $[0/90/90/0]_{3s}$ stringer stacking sequence.

The SIEI surface in Figure 9 shows that the optimum super-stringer design is not obtained by simply minimising both the skin and stringer ply thicknesses as expected. Instead,

the maximum value, 7.97×10^5 J/m^2, is reached at $t_{\text{skin}} = 0.3$ mm and $t_{\text{stringer}} = 0.1$mm. This indicates that, for the selected skin and stringer layups, a moderate increase in skin thickness initially improves the stored contact energy more rapidly than the associated thickness penalty, so that the SIEI rises until an optimum is reached. A clear change in behaviour can also be observed depending on the stringer thickness. For relatively large stringer thicknesses, the optimum skin thickness shifts towards the minimum admissible value. In this region, the thickness penalty associated with the already heavy stringer becomes dominant, so any further increase in skin thickness reduces the SIEI. Consequently, the best laminate configuration for the super-stringer is summarised in Table 6.

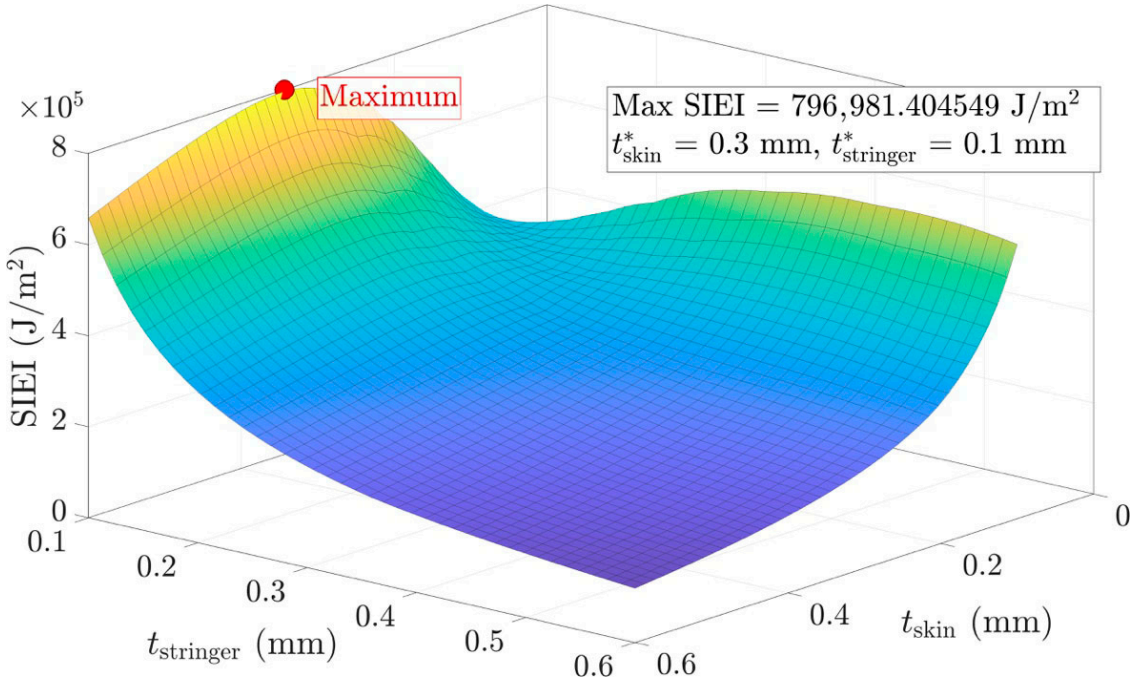

Figure 9. SIEI as a function of skin and stringer ply thickness (skin $[0/90/90/0]_{3s}$, stringer $[45/-45/0/90]_{3s}$).

Table 6. Best super-stringer configuration.

Component	Stacking Sequence	Ply Thickness
Skin	$[45/-45/0/90]_{3s}$	0.3 mm
Stringer	$[0/90/90/0]_{3s}$	0.1 mm

5. Conclusions

This work has presented a low-fidelity analytical framework for the impact assessment and preliminary design of stringer-stiffened composite panels under low-velocity impact. The study combined First Order Shear Deformation Theory with a two-degree-of-freedom spring–mass impact model, and extended the approach to a super-stringer configuration by idealising the stringer as a Euler–Bernoulli beam whose bending rigidity is transferred to the skin mid-surface through the parallel axis theorem. In addition, a Specific Impact Energy Index (SIEI) was introduced to compare candidate laminate configurations on the basis of elastic energy storage efficiency penalised by total laminate thickness. In this sense, the paper does not merely apply existing impact formulations, but provides an integrated analytical methodology that links laminate stiffness properties directly to the impact-driven selection of a stiffened configuration.

The first main outcome of the work is that the proposed analytical model is sufficiently accurate for preliminary design and for identifying governing parameter trends. Validation

against a published reference case showed good approximation, reproducing the correct order of magnitude, time scale and general force-history evolution. The comparison also clarified that the discrepancies in waveform shape are mainly associated with the modal superposition inherent to the two-degree-of-freedom spring–mass model, which may generate oscillatory beat-like responses depending on the relative participation of the two natural modes. Even so, the model proved adequate for ranking laminate responses and for capturing the physical dependency of the impact response on the underlying stiffness terms.

The study showed that a simple procedural design strategy can identify an efficient super-stringer laminate without using expensive optimisation algorithms. The best configuration was obtained with a $[0/90/90/0]_{3s}$ stringer and a $[45/-45/0/90]_{3s}$ skin. Thickness optimisation revealed that the maximum SIEI is achieved with a skin ply thickness of 0.3 mm and a stringer ply thickness of 0.1 mm, giving 7.97×10^5 J/m^3. This confirms that the optimum is not obtained by simply minimising both thicknesses, but by balancing the gain in stored impact energy against the thickness penalty. Overall, the work demonstrates that a low-cost analytical framework can provide effective preliminary design guidance for stiffened composite panels, while also highlighting the limitations of the current elastic and linearised formulation.

The proposed model is shown to be sufficiently reliable for preliminary design screening and identification of governing parameter trends. However, in the case of the stiffened configuration, the current level of validation remains numerical rather than experimental, and the conclusions should therefore be interpreted within the scope of a low-fidelity, elastic and linearised analytical framework.

A priority extension of the present work is the experimental validation of the super-stringer configuration under controlled low-velocity impact conditions. This would allow direct assessment of the model accuracy in terms of peak force, contact duration and energy transfer, and would clarify the extent to which the oscillatory response predicted by the TDOF formulation affects the agreement with physical tests.

Author Contributions: Conceptualization, J.J.C.R. and H.G.; Methodology, J.J.C.R. and H.G.; Software, J.J.C.R.; Validation, J.J.C.R.; Formal analysis, J.J.C.R.; Investigation, J.J.C.R.; Data curation, H.G.; Writing—original draft, J.J.C.R.; Writing—review & editing, H.G.; Visualization, H.G.; Supervision, H.G.; Project administration, H.G.; Funding acquisition, H.G. All authors have read and agreed to the published version of the manuscript.

Funding: This research did not receive any specific grant from funding agencies in the public, commercial, or not-for-profit sectors.

Data Availability Statement: The data presented in this study are available on request from the corresponding author.

Conflicts of Interest: The authors declare no conflict of interest.

References

1. Greszczuk, L.B. Damage in composite materials due to low velocity impact. In *Impact Dynamics*; Zukas, J.A., Nicholas, T., Swift, H.F., Greszczuk, L.B., Curran, D.R., Eds.; John Wiley & Sons: Hoboken, NJ, USA, 1982; pp. 55–94.
2. Shivakumar, K.N.; Elber, W.; Illg, W. Prediction of impact force and duration due to low-velocity impact on circular composite laminates. *J. Appl. Mech.* **1985**, *52*, 674–680. [CrossRef]
3. Tan, T.M.; Sun, C.T. Use of Statical Indentation Laws in the Impact Analysis of Laminated Composite Plates. *J. Appl. Mech.* **1985**, *52*, 6–12. [CrossRef]
4. Gong, S.W.; Lam, K.Y. Transient response of stiffened composite plates subjected to low velocity impact. *Compos. Part. B Eng.* **1999**, *30*, 473–484. [CrossRef]
5. Olsson, R. Analytical prediction of large mass impact damage in composite laminates. *Compos. Part A Appl. Sci. Manuf.* **2001**, *32*, 1207–1215. [CrossRef]

6. Abdalla, A.B.; Israr, H.A.; Zaki, M.I.N.; Tamin, M.N.; Ahmad, Z. Analytical Modelling and Experimental Validation of Low-velocity Impact Responses in Unidirectional CFRP Composite Using FSDT and TDOF Approaches. *J. Mek.* **2025**, *48*, 97–110. [CrossRef]
7. Tan, R.; Guan, Z.; Sun, W.; Liu, Z.; Xu, J. Experiment investigation on impact damage and influences on compression behaviors of single T-stiffened composite panels. *Compos. Struct.* **2018**, *203*, 486–497. [CrossRef]
8. Vescovini, A.; Li, C.X.; Malverti, C.; Jin, B.C.; Manes, A. Low-velocity impact behavior of flat and tapered Single–Double composites specimens. *Compos. Struct.* **2025**, *355*, 118823. [CrossRef]
9. Vaziri, R.; Quan, X.; Olson, M.D. Impact analysis of laminated composite plates and shells by super finite elements. *Int. J. Impact Eng.* **1996**, *18*, 765–782. [CrossRef]
10. Delfosse, D.; Vaziri, R.; Pierson, M.; Poursartip, A. Analysis of the non-penetrating impact behaviour of CFRP laminates. In Proceedings of the 9th International Conference on Composite Materials, Madrid, Spain, 12–16 July 1993; pp. 366–373.

Disclaimer/Publisher's Note: The statements, opinions and data contained in all publications are solely those of the individual author(s) and contributor(s) and not of MDPI and/or the editor(s). MDPI and/or the editor(s) disclaim responsibility for any injury to people or property resulting from any ideas, methods, instructions or products referred to in the content.

https://dspace.org/

Analytical development of impact response of stiffened composite panel with optimum structural behaviour

Cruz Reyes, José Juan; Ghasemnejad, Hessam

2026-04
MDPI
https://doi.org/10.3390/jcs10040213
Cruz Reyes JJ, Ghasemnejad H. (2026) Analytical development of impact response of stiffened composite panel with optimum structural behaviour. Journal of Composites Science, Volume 10, Issue 4, April 2026, Article number 213

Downloaded from a DSpace repository. https://dspace.org/